Chinese Chemical Letters 33 (2022) 1117–1130

Contents lists available at ScienceDirect

Chinese Chemical Letters

journal homepage: www.elsevier.com/locate/cclet

Direct catalytic nitrogen oxide removal using thermal, electrical or solar energy

Xiaohu Zhang, Lixiao Han, Hao Chen, Shengyao Wang*

College of Science, Huazhong Agricultural University, Wuhan 430070, China

ARTICLE INFO

Article history:
Received 10 April 2021
Revised 26 May 2021
Accepted 14 July 2021
Available online 23 July 2021

Keywords:
NO removal
Photo-catalysis
Electro-catalysis
Thermo-catalysis
Oxidation
Reduction

ABSTRACT

Considering the significant importance in both ecological and environmental fields, converting nitrogen oxide (NO_x, especially NO) into value-added NH_3 or harmless N_2 lies in the core of research over the past decades. Exploring catalyst for related gas molecular activation and highly efficient reaction systems operated under low temperature or even mild conditions are the key issues. Enormous efforts have been devoted to NO removal by utilizing various driving forces, such as thermal, electrical or solar energy, which shine light on the way to achieve satisfying conversion efficiency. Herein, we will review the state-of-the-art catalysts for NO removal driven by the above-mentioned energies, including a comprehensive introduction and discussion on the pathway and mechanism of each reaction, and the recent achievements of catalysts on each aspect. Particularly, the progress of NO removal by environmentally friendly photocatalysis and electrocatalysis methods will be highlighted. The challenges and opportunities in the future research on the current topic will be discussed as well.

1. Introduction

The global environment and human's respiratory system are being affected by NO_x (NO and NO_2) pollution, which is mainly produced from large utility boilers, industrial boilers, municipal waste plants, vehicles and incinerators [1–6]. At present, the most popular way of NO removal is selective catalytic reduction (SCR) of NO_x with NH_3 (NH_3-SCR) to harmless N_2 and H_2O which was initially developed by Hitachi Zosen in Japan at ~1970 [7–9]. Generally, TiO_2 supported V-, W- or Mo-based oxides are the most widely used industrial catalyst under high temperature (> 200 °C) and 80–100% NO_x emissions can be reduced by this technology. Although some other types of catalyst, such as zeolite-supported Cu [1,10] and Mn, Cu-based oxides [11,12], can work under lower temperatures, dilute NO (ppb level) can not be reduced by this method effectively and consumption of valuable NH_3 makes it as an undesirable way.

Recently, environmentally friendly semiconductors-based photocatalysis (especially photocatalytic oxidation) using solar energy has received considerable attention in view of its potentiality for efficient pollutants [13–16] and dilute NO removal especially in ppb level (~ 600 ppb) [17,18]. Up till now, numerous photocatalytic materials, such as TiO_2 [19–21], Bi-based metal oxides [22–27], g-C_3N_4 [28–33] and heterojunctions [34–37], all exhibit excellent NO removal efficiency and selectivity. In this process, NO removal is mostly supposed to take place via an Eley-Rideal mechanism, through which O_2 is firstly activated by photogenerated e^- with formation of reactive oxygen species (ROS) and then NO will react with ROS [38]. That is, NO is inactivated in this mechanism which is disadvantageous in photocatalytic NO oxidation. Generally, enhancing e^-/h^+ separation through bandgap engineering, doping or heterojunction fabrication and facilitating O_2 activation by construction of surface oxygen vacancies (OVs) are two mainstream strategies for designing photocatalyst to improve NO removal activity. From the thermodynamically point of view, activated NO (NO^+, a better electron acceptor) would strongly interact with the $^{\bullet}O_2^-$ to produce nitrate via dual-site route through Langmuir-Hinshelwood (L-H) mechanism as compared with the inactivated NO [38]. Inspired by the fact that Au nanoparticles with unfilled orbital electronic structure are capable of binding with NO possessing lone pair electrons, a bicomponent Au/CeO_2 photocatalyst with dual-sites for adsorption/activation of O_2 and NO simultaneously was designed by Shang *et al.* to improve the photocatalytic NO purification efficiency [38]. Compared with photocatalytic NO oxidation reaction, reducing NO to N_2 or even NH_3 synthesis through photocatalysis or electrocatalysis are rarely investigated [39–44]. How-

* Corresponding author.
E-mail address: wangshengyao@mail.hzau.edu.cn (S. Wang).

https://doi.org/10.1016/j.cclet.2021.07.034
1001-8417/

Fig. 1. NO_x removal is driven by thermo-, photo- and electro-catalysis processes.

ever, these types of reactions would be more promising in consideration of the high value of NH_3 and the lack of species such as NO_3^- occupying active sites on the surface of materials which often result in the inactivation of photocatalyst.

Although NH_3-SCR has been successfully applied in industry for almost 50 years, photocatalytic NO oxidation has been investigated for more than 10 years, and some more interesting NO reduction reactions have emerged very recently, a systematic review on the field of NO removal has lacked as far as we know. Generally, the key scientific issues related to NO removal lies in: (1) Exploring more efficient catalyst working under ambient conditions along with high selectivity. (2) Mechanism investigation such as NO removal pathway and structure-activity relationship. (3) Active sites construction and reactant, especially NO molecule, activation. This short review mainly summarizes the reported literature in both NO oxidation and NO reduction reactions (Fig. 1) by series of energy input. And then, some critical issues are discussed. Finally, some prospective strategies are highlighted. The objective of this review is to provide a clear horizon on this field and guide the rational design for more effective catalysts.

2. Overview on reactions of NO removal

2.1. Reduction of NO

2.1.1. Selective reduction of NO with NH_3 (NH_3-SCR)

The NH_3-SCR technology proceeds according to following Eqs. 1 and 2:

$$4NO + 4NH_3 + O_2 = 4N_2 + 6H_2O \quad (1)$$

$$2NO_2 + 4NH_3 + O_2 = 3N_2 + 6H_2O \quad (2)$$

Taking supported V_2O_5-WO_3/TiO_2 catalysts which are the most widely used and investigated industrial catalysts for these SCR applications as for example, NH_3-SCR proceeds *via* a surface Mars-van Krevelen mechanism as follows (Eqs. 3–8) involving the participation of weakly adsorbed NO with surface adsorbed NH_x species (mostly NH_4^{+*} species on Brønsted acid sites, and some surface NH_3^* species can convert to surface NH_4^{+*} species in the presence of moisture) [7]:

$$\left[V^{5+}OH + V^{5+}=O\right]^* + NH_3 \rightarrow \left[V^{5+}O^{-}\text{--}HN^{+}H_3 + V^{5+}=O\right]^* \quad (3)$$

$$\left[V^{5+}O^{-}\text{--}HN^{+}H_3 + V^{5+}=O\right]^* \rightarrow \left[V^{5+}O^{-}\text{--}{}^{+}H_3N\text{--}HOV^{4+}\right]^* \quad (4)$$

$$\left[V^{5+}O^{-}\text{--}{}^{+}H_3N\text{--}HOV^{4+}\right]^* + NO \rightarrow \left[V^{5+}O^{-}\text{--}{}^{+}H_3NNO\text{--}HOV^{4+}\right]^* \quad (5)$$

$$\left[V^{5+}O^{-}\text{--}{}^{+}H_3NNO\text{--}HOV^{4+}\right]^* \rightarrow \left[V^{5+}O^{-}\text{--}{}^{+}H_3NNO\right]^* + \left[HOV^{4+}\right]^* \quad (6)$$

$$\left[V^{5+}O^{-}\text{--}{}^{+}H_3NNO\right]^* \rightarrow \left[V^{5+}OH\right]^* + N_2 + H_2O \quad (7)$$

$$4\left[HOV^{4+}\right]^* + O_2 \rightarrow 4\left[V^{5+}{=}O\right]^* + 2H_2O \quad (8)$$

The rate-determining step investigated by density functional theory (DFT) methods involves breaking of an N–H bond during the course of formation or decomposition of the surface NO-NH_x reaction intermediate complex. In addition, moisture that is the H_2O concentration plays a significant role in the SCR reaction and inhibiting oxidation of SO_2 to SO_3 should be taken into consideration [7].

2.1.2. Electrocatalytic reduction reaction of NO (NORR)

Although NO can be converted into harmless N_2 by above SCR technology, valuable NH_3 (an essential chemical substance to produce fertilizers) is consumed. Electrochemical ammonia synthesis from N_2 (NRR) or NO_3^- reduction has been widely reported [45], and it is found that NO can be reduced from exhausted gas to ammonia by coupling NO removal and ammonia synthesis electrochemically [41,42]. In addition, the NH_3 synthesis activity and selectivity in NORR is higher than that of NRR which is usually limited by N_2 dissociation and competitive HER (hydrogen evolution reaction). Generally, NORR follows proton-coupled electron transfer process reported in literature (Eqs. 9–18):

Route 1 [43]:

$$NO(g) + H^+ + e^- \rightarrow NOH^* \quad (9)$$

$$NOH^* + H^+ + e^- \rightarrow N^* + H_2O \quad (10)$$

$$N^* + H^+ + e^- \rightarrow NH^* \quad (11)$$

$$NH^* + H^+ + e^- \rightarrow NH_2{}^* \quad (12)$$

$$NH_2{}^* + H^+ + e^- \rightarrow NH_3{}^* \quad (13)$$

Route 2 [44]:

$$NO(g) + H^+ + e^- \rightarrow NOH^* \quad (14)$$

$$NOH^* + H^+ + e^- \rightarrow NHOH^* \quad (15)$$

$$NHOH^* + H^+ + e^- \rightarrow NH_2OH^* \quad (16)$$

$$NH_2OH^* + H^+ + e^- \rightarrow NH_2{}^*H_2O \quad (17)$$

$$NH_2{}^*H^+e^- \rightarrow NH_3{}^* \quad (18)$$

2.1.3. Photocatalytic NORR

Compared with NH_3-SCR and electrocatalytic NORR, direct dissociation of NO into N_2 and O_2 by semiconductor based photocatalyst such asTiO_2 is promising. Generally, metal doping or oxygen vacancies formation is necessary for photocatalytic NO reduction [39,40].

2.2. Oxidation of NO

2.2.1. Oxidation of NO by strong oxidants

Generally, NO can be oxidized into NO_2 and NO_3^- by strong oxidants such as H_2O_2 and O_3 [46–48]. Take H_2O_2 as example, the standard electrode potentials of H_2O_2 (1.770 V) and $HO^•$ (2.800 V, produced from H_2O_2 with UV light irradiation) are far higher than those of NO_2/NO (1.049 V), NO_3^-/NO (0.957 V), NO_2^-/NO (0.460 V), and NO_3^-/NO_2^- (0.835 V), which demonstrates the feasibility of NO oxidation according to the following Eqs. 19–27:

Route 1: without irradiation

$$H_2O_2 + NO \rightarrow NO_2 + H_2O \quad (19)$$

$$3H_2O_2 + 2NO \rightarrow 2NO_3^- + H_2O + 2H^+ \quad (20)$$

$$H_2O_2 + NO_2 \rightarrow 2NO_3^- + 2H^+ \quad (21)$$

Route 2: with irradiation

$$H_2O_2 + h\nu \rightarrow 2HO^• \quad (22)$$

$$HO^• + NO \rightarrow NO_2^- + H^+ \quad (23)$$

$$HO^• + NO \rightarrow NO_2 + H^• \quad (24)$$

$$2HO^• + NO \rightarrow NO_3^- + H^+ + H^• \quad (25)$$

$$2HO^• + NO_2^- \rightarrow NO_3^- + H_2O \quad (26)$$

$$2HO^• + NO_2 \rightarrow NO_3^- + H^+ \quad (27)$$

2.2.2. Photocatalytic oxidation of NO

Reactive oxygen species (ROS, such as $^•OH$, $^•O_2^-$, $^1O_2$) and holes (h^+ or O^-) play significant roles in semiconductor-based photocatalytic oxidation of NO. Up till now, two representative mechanisms are proposed as follows: (1) $^•O_2^-$ originated from the reaction of oxygen and photogenerated electrons mainly participated in the oxidation of NO to NO_2, which was further oxidized to NO_3^- by $^•OH$ and holes (Eqs. 28-33); (2) NO was directly oxidized to NO_3^- by $^•O_2^-$, and partial NO oxidation for NO_2 generation was normally attributed to $^•OH$ and holes (Eqs. 28, 34-35). Generally, tuning the formation of oxygen reactive species in catalyst design is significant.

Route 1 [23,49,50]:

$$O_2 + e^- \rightarrow^• O_2^- \quad (28)$$

$$^•O_2^- + NO + 2H^+ \rightarrow NO_2 + H_2O \quad (29)$$

$$2h^+ + NO + H_2O \rightarrow NO_2 + H^+ \quad (30)$$

$$2^•OH + 2NO \rightarrow 2NO_2 + H_2O \quad (31)$$

$$h^+ + NO_2 + H_2O \rightarrow NO_3^- + H^+ \quad (32)$$

$$^•OH + NO_2 \rightarrow NO_3^- + H^+ \quad (33)$$

Route 2 [17,18]:

$$^•O_2^- + NO \rightarrow NO_3^- \quad (34)$$

$$NO + h^+/^•OH \rightarrow NO_2 \quad (35)$$

3. Recent developments in NO removal

3.1. NH_3-SCR

As mentioned above, numerous researches have been focused on supported V_2O_5-WO_3/TiO_2 catalysts, and series of impact parameters such as catalyst synthesis, molecular structures, surface acidity, catalytic active sites, surface reaction intermediates, rate determining-step, and reaction kinetics have been investigated [7,51]. However, this type of catalysts needs high reaction temperature (> 300°C), which is not suitable of some industrial boilers with lower outlet temperature.

Recently, some other type of catalysts including zeolite-supported Cu and Fe and other transition metal oxides have been developed for NH_3-SCR technology to satisfy different application scenarios [1,8–12,52]. To enhance the oxidation and SO_2-tolerant property of catalyst, a mesoporous $MnCeSmTiO_x$ amorphous mixed oxides is constructed by coprecipitation method [11]. As shown in Fig. 2a, the NO conversion could reach nearly 100% at 140–320 °C and maintain > 90% at 400 °C and a gas hourly space velocity of 80,000 h^{-1}. More importantly, the selectivity of N_2 could be maintained at ≈100% at 100–320 °C and stay at > 90% up to 400 °C (Fig. 2b). In addition, the influence of adding SO_2 and water vapor which are inevitable in exhaust and flue gases on the catalytic performance were investigated. As can be seen in Figs. 2c and d, slight decrease of NO removal efficiency was observed for $MnCeSmTiO_x$ catalyst, which maintained better activity than that of $MnCeTiO_x$, indicating the excellent SO_2/H_2O-tolerant. It is found that the NH_3-SCR follows Langmuir-Hinshelwood mechanism, and synergistic effect of the Lewis acid sites and oxidation catalytic-sites play important roles in the reaction. Sm doping can increase transfer electrons to Mn^{4+} and Ce^{4+}, which facilities the formation of active adsorbed NO_2 (bidentate nitrate, and bridging nitrate intermediates), enhances the NO conversion at low temperatures and suppresses SO_2 poisoning.

Using MOFs as the precursor [12], a series of Fe-Doped Mn_3O_4 ($Fe_xMn_{3-x}O_4$) nanoparticles possessing efficient $Fe_{oct(octahedral)}$-O-$Mn_{tet(tetrahedral)}$ site were synthesized and exhibited a NO conversion up to 90% at 180 °C in an ultrahigh gas hourly space velocity (GHSV) of 400,000 h^{-1}. DFT calculations were carried out to obtain insights on how the catalytic activity was affected by Fe_{oct}. Interestingly, the formation of oxygen vacancy (Fig. 3a) was the rate-determining step of NO oxidation. With the replacement of Mn_{oct} by Fe_{oct}, the required free-energy change for NO-to-NO_2 oxidation all decreased to some extent, and Fe_{oct}-O-Mn_{tet} is the most efficient active site. It should be note that the charge density between M_{oct} and O were decreased after the replacement of M_{oct} by Fe_{oct}, which facilitated the formation of OV (Fig. 3b). The enhanced NO oxidation can trigger the "fast SCR" reaction, thus leading to the boosted NH_3-SCR performance.

Although NH_3-SCR technology can treat high concentration NO_x emissions (several hundred ppm, *i.e.*, 500 or 600 ppm) with high conversion efficiency, they are not economically for low concentration NO_x (ppb level) purification in atmosphere since this technology can just work under high temperature (> 250 °C). More importantly, the NH_3-SCR process consumes high-cost and valuable NH_3 which is usually synthesized by extremely energy dependent Haber–Bosch process. By the way, NH_3-SCR is not suitable for many industrial boilers, which have lower outlet temperature and contain impurities including SO_2 and H_2O. In addition, the adsorption and activation of NH_3 is thought to be the first step in NH_3-SCR, therefore, exploiting catalyst that can active NH_3 and NO simultaneously should be the aim in future to realize NO removal under lower temperature and even mild condition. In a word, NH_3-SCR has been successfully applied in industry for almost 50 years, and will be still the dominant technology for high concentration

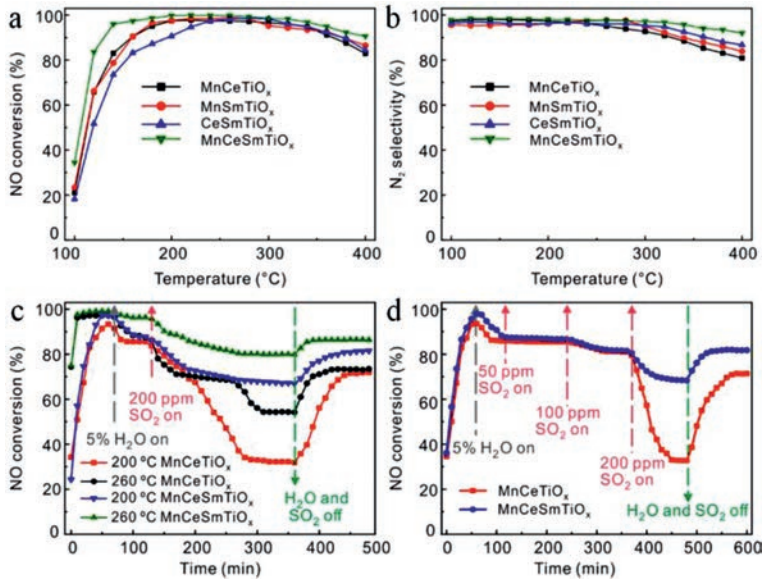

Fig. 2. NO conversion (a) and N_2 selectivity (b) of $MnCeTiO_x$, $MnSmTiO_x$, $CeSmTiO_x$, and $MnCeSmTiO_x$ catalysts. H_2O and SO_2 tolerance test of $MnCeTiO_x$ and $MnCeSmTiO_x$ catalysts at different temperatures (c) and introducing SO_2 with different concentrations (d) [reaction conditions: $v(NO) = v(NH_3) = 500$ ppm, $v(O_2) = 5$ vol %, balance Ar, and GHSV = 80,000 h^{-1}. Copied with permission [11]. Copyright 2020, American Chemical Society.

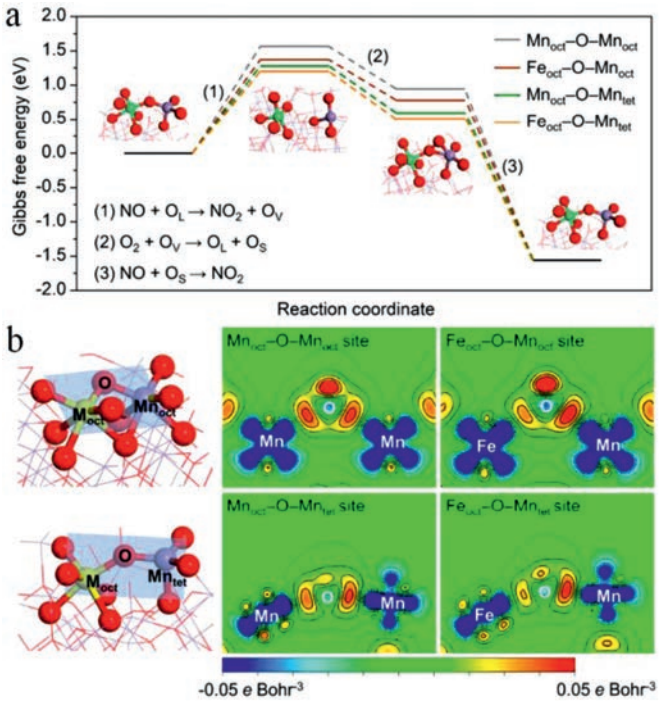

Fig. 3. (a) Gibbs free energy (400 K) diagram over NO-to-NO_2 oxidation based on Mars and van Krevelen (MvK) mechanism and (b) charge density difference contour plots for Mn_{oct}-O-Mn_{oct}, Fe_{oct}-O-Mn_{oct}, Mn_{oct}-O-Mn_{tet} and Fe_{oct}-O-Mn_{tet} sites. Copied with permission [12]. Copyright 2020, American Chemical Society.

NO_x removal in a long time until novel environmental friendly methods operating under mild conditions can be practically utilized.

3.2. Electrocatalytic NORR

Different form the above NH_3-SCR process, it was reported that that NO could be reduced to NH_3 instead of N_2 or other inorganic compounds over Pt (100) or Co-N_4 single site based on DFT results [41,42], and a similar conversion pathway was proposed as Fig. 4 [41]. This finding is promising in terms of coupling NO removal and NH_3 synthesis, which convert exhausted gas to NH_3 directly. In fact, Long *et al.* found that Cu exhibit higher activity for NORR than NRR, as well as superior NH_3 selectivity relative to N_2 and H_2 production, and the designed Cu foam electrode achieved a record-high NH_3 production rate of 517.1 μmol cm^{-2} h^{-1} with a Faradaic efficiencies (FE) of 93.5% at −0.9 V *vs.* RHE accompanied a significantly enhanced current density (Figs. 5a-c) [43]. NH_3 is always the dominant product at different tested potentials with high FE (Figs. 5d and e). Moreover, the turnover frequency (TOF) increases from 2630 s^{-1} to 7840 s^{-1} with the potential varying from 0.3 V to–1.2 V (Fig. 5f). Additionally, associative Heyrovsky distal-O pathway (AHDO) NORR pathway (Eqs. 9-13) was proposed based on DFT result.

To avoid direct use of highly concentrated NO gas, a rationally designed electrolyte containing the EDTA-Fe^{2+} metal complex (EFeMC) which is known for its rapid NO capture ability was adopted to selectively produce NH_3 by NORR [44]. Fig. 6a gave the H-type electrolysis cell that was used for NORR. The electrolyte is Ar gas-purged or NO gas saturated 50 mmol/L EFeMC in a natural-pH phosphate buffer solution (PBS), noted as PBS-MC_{50}-Ar and PBS-MC_{50}-NO_s respectively. In addition, a nanostructured Ag electrode was selected because of its ability to sufficiently suppress the HER, while Pt foil and glassy carbon (GC) were also used as cathode materials for control experiments.

The quite distinguished LSV features in Fig. 6b indicated that HER was spontaneous and dominant reaction on Pt, while NO@EFeMC species was involved in the electrochemical reaction on Ag and GC. As a result, nearly ~100% FE for NH_3 production in potential ranges of −0.15 V to −0.29 V_{RHE} and −0.29 V to −0.34 V_{RHE} for Ag and GC electrode were observed respectively, and the economic analysis is carried out using itemized cost estimation, indicating its market competitive ($0.03 k/Wh).

Although the above pioneering reports present a new scenario for reusing the exhaust NO gas, the real NO reduction mechanism and more advanced materials with higher efficiency should be further explored. In addition, electrocatalytic converting NO into

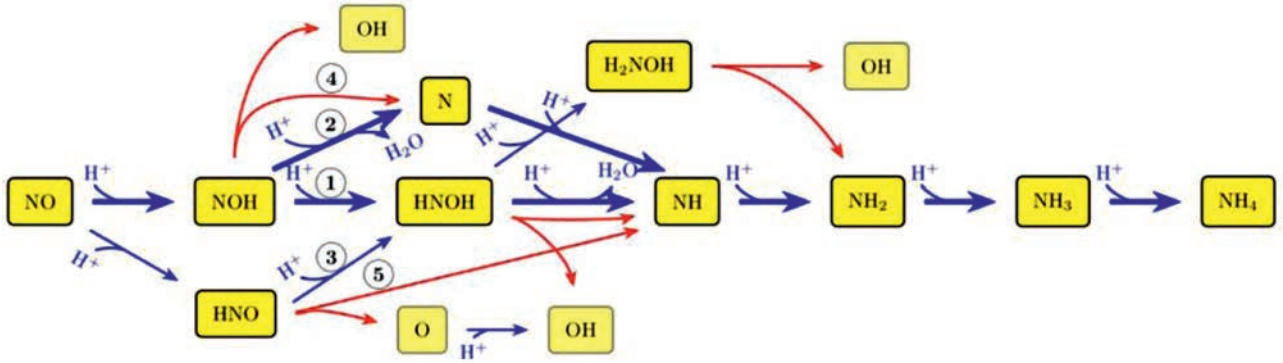

Fig. 4. Most probable pathways found in kinetic Monte Carlo (kMC) simulations are indicated by numbers within circles. Blue arrows refer to electrochemical steps and red arrows to chemical steps. Thrick blue arrows mark the most probable pathways. To simplify the notation, $(H^+ + e^-)$ is expressed as H^+. Copied with permission [41]. Copyright 2017, American Chemical Society.

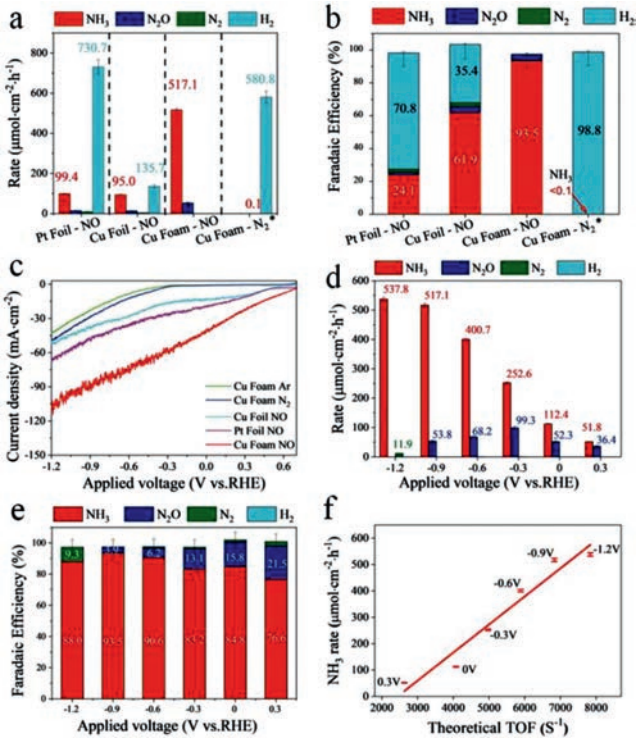

Fig. 5. Experiments of NORR and NRR over different catalysts and theoretical microkinetic simulation. Reaction rate (a) and Faradaic efficiency (b) for NORR on a Pt foil, Cu Foil, and Cu foam for 600 s, and NRR over Cu foam for 2 h at -0.9 V *vs.* RHE. (c) Linear Sweep Voltammetry (LSV) for Pt foil, Cu foil and Cu foam in NO-saturated 0.25 mol/L Li_2SO_4 Cu foam in Ar or N_2-saturated 0.25 mol/L Li_2SO_4 acquired with a scan rate of 10 mV/s at 25 °C. Reaction rate (d) and Faradaic efficiency (e) of NORR on Cu foam at varying potentials. (f) The measured ammonia production rates over the Cu foam plotted as theoretical TOF at different potentials. Copied with permission [43]. Copyright 2020, John Wiley & Sons, Inc.

value-added NH_3 can be operated under mild condition which is energy saving. However, high flow rate of pure NO gas (*i.e.*, 5–30 mL/min) are required due to the low solubility of NO in water. By the way, the above-mentioned electrocatalyst can directly active NO molecule, which can provide scientists with new material designing direction in other NO removal fields like photocatalysis and thermocatalysis, where NO is usually considered inactivated. The electrocatalytic NO reduction is promising in consideration of the high value product of NH_3 and the controlled selectivity by tunable bias voltage.

3.3. Photocatalytic NORR

Compared to thermo- and electro-catalysis, environmentally friendly semiconductor-based photo-catalysis using solar energy is attractive. S. Roy *et al.* found that N_2 and N_2O could be detected when NO was passed over Pd^{2+} doped TiO_2 ($Ti_{0.99}Pd_{0.01}O_{1.99}$) catalyst under UV light irradiation [39].

In general, 45% dissociation of NO was observed in the first run with decreased efficiency in the following runs, and the NO conversion efficiency could be maintained at ~80% when mixture of CO and NO gas was adopted. In addition, the creation of oxide ion vacancy in $Ti_{0.99}Pd_{0.01}O_{1.99}$ was primary requirement for NO reduction, and the presence of CO seemly inhibited partial conversion of NO to NO_2 which would block the oxide ion vacancy sites. To inhibit the formation of NO_2, Fe^{3+} doped TiO_2 (Fe-TiO_2, Fig. 7) with oxygen vacancies which was stabilized by Fe^{3+} were also reported to act as catalytic centers that capture the oxygen end of the NO molecules and further dissociate NO into N_2 and O_2 (4.5% conversion efficiency), and the photoinduced reduction of Fe^{3+} to Fe^{2+} almost completely suppressed the formation of NO_2 and thus enhanced the selectivity of the reaction for N_2 formation [40].

3.4. Oxidation of NO by strong oxidants

Hao *et al.* evaluated the macrokinetics of NO oxidation by vaporized H_2O_2 association with ultraviolet light, and found the method was more effective than conventional UV-H_2O_2 reaction system [48]. In addition, advanced oxidation process based on UV-H_2O_2 was reported to simultaneously remove NO and SO_2 from coal-fired flue gas with high efficiency.

3.5. Photocatalytic oxidation of NO

Although rare literatures are reported for photocatalytic NO reduction, numerous works are focused on photocatalytic NO oxidation (Table 1) [2–4,6,17–19,21–25,28–31,34–38,53–106]. To clarify the collaboration of different type of ROS in photocatalytic NO oxidation, Ding *et al.* designed Bi self-doped Bi_2MoO_6 to modulate the ROS generation [49]. Based on DFT calculation, band-position and series of photoactivities with different scavengers analyses, they found that $^{\bullet}O_2^-$ could improve the oxidation of NO to NO_2 as well as $^{\bullet}OH$ and h^+ mainly contributed to the further oxidation of NO_2 to NO_3^-. Generally, ultrathin 2D materials possess unique electron transfer property. In addition, their band-gap and redox potential can be modulated by foreign atom doping. For example, Wang *et al.* [50] designed ultrathin (001) facet exposed Bi_2MoO_6

Table 1
Partial recent progress in photocatalytic NO oxidation.

Material type	Photocatalysts	Reaction conditions	NO removal efficiency (%)	NO_3^- selectivity (%)	Ref.
Metal oxides based materials	$Bi@Bi_2O_3$ nanospheres	flow reactor, xenon lamp, > 420 nm	~40	~100	[2]
	$(BiO)_2CO_3$	flow reactor, xenon lamp, > 420 nm	55.6	~100	[3]
	La-doped $(BiO)_2CO_3$	flow reactor, tungsten halogen lamp, > 420 nm	49.8	82.2	[4]
	$BiOBr/SnO_2$	flow reactor, tungsten halogen lamp, > 420 nm	50.3	–	[6]
	$BiOBr/La_2Ti_2O_7$	flow reactor, tungsten halogen lamp, > 420 nm	43	–	[22]
	Bi_2MoO_6	flow reactor, visible LEDs	62.9	93.61	[23]
	$CaSO_4$-BiOI	flow reactor, a lamp (420–780 nm)	54.4	–	[24]
	$(BiO)_2CO_3$/graphene	homemade NO photodegraded testing system	~50	–	[25]
	BiOCl	flow reactor, > 420 nm	36.5	–	[53]
	$BiOBr_{0.5}I_{0.5}$/BiOI	flow reactor, xenon lamp, > 420 nm	36.2	–	[54]
	$Bi_2Mo_3O_{12}@Bi_2O_2CO_3$	flow reactor, tungsten halogen lamp, > 420 nm	~35	–	[55]
	$SrTiO_3$/BiOI	flow reactor, tungsten halogen lamp, > 420 nm	59	–	[56]
	α-$Bi_2O_3/CuBi_2O_4$	flow reactor, xenon lamp, > 420 nm	30	93.31	[37]
	Bi-$(BiO)_2CO_3$	flow reactor, tungsten halogen lamp, > 420 nm	40.8	–	[57]
	Bi-$BiPO_4$	flow reactor, xenon lamp, > 420 nm	32.8	–	[58]
	Bi-BiOI/graphene	flow reactor, xenon lamp, > 420 nm	51.8	–	[59]
	BiOCl/PPy	flow reactor, tungsten halogen lamp, > 420 nm	28	~100	[60]
	Au/La-Bi_5O_7I	flow reactor, xenon lamp, > 420 nm	42.7	–	[61]
	Bi_2WO_6/BiOI	flow reactor, xenon lamp, > 420 nm	40	–	[62]
	Bi/BiOI/$(BiO)_2CO_3$	flow reactor, tungsten halogen lamp, > 420 nm	50.7	–	[63]
	Bi/BiOI	flow reactor, tungsten halogen lamp, > 420 nm	40.8	–	[64]
	C-Bi_2WO_6	flow reactor, tungsten halogen lamp, > 420 nm	58	–	[65]
	BiOBr/BiOI	flow reactor, xenon lamp, > 420 nm	57	–	[66]
	$BiSbO_4$	flow reactor, tungsten halogen lamp, > 420 nm	42	–	[67]
	Bi/$Bi_2O_{2-x}CO_3$	flow reactor, xenon lamp, > 420 nm	50.5	98	[68]
	Bi /$Bi_2O_2SiO_3$	flow reactor, tungsten halogen lamp, > 420 nm	50.2	–	[69]
	BiOCl	flow reactor, UV light, 360 nm	41	–	[70]
	BiOCl	flow reactor, xenon lamp	60	90	[17]
	Bi_2WO_6	flow reactor, tungsten halogen lamp, > 420 nm	47	–	[71]
	Bi_2WO_6	flow reactor, tungsten halogen lamp, > 420 nm	55	–	[72]
	BP/ Bi_2WO_6	flow reactor, xenon lamp	67	–	[73]
	$(BiO)_2CO_3$	flow reactor, tungsten halogen lamp, > 420 nm	56	–	[74]
	$SrCO_3$-BiOI	flow reactor, a lamp (420–700 nm)	48.3	–	[75]
	$BaCO_3$/BiOI	flow reactor, a lamp (420–780 nm)	47.5	–	[76]
	$Bi_2O_3/Bi_2O_2CO_3$	flow reactor, xenon lamp	44	–	[77]
	BiOCl	flow reactor, xenon lamp or UV light	70	99	[18]
	ZnO	flow reactor, LED	36.7	–	[78]
	La-ZnO	flow reactor, UV light, 360 nm	53.6	–	[79]
	$(Zn_{1+x}Ge)(N_2O_x)$	flow reactor, high pressure mercury lamp	40	–	[80]
	N–TiO_2	flow reactor, xenon lamp, > 420 nm	100	–	[81]
	Au/CeO_2	flow reactor, xenon lamp, > 400 nm	65	–	[38]
	Fe-TiO_2	flow micro-reactor, xenon lamp, > 420 nm	100	–	[19]
	Blue TiO_2	flow reactor, xenon lamp, > 400 nm	63	99	[21]
	Ag-TiO_2	flow reactor, xenon lamp, > 400 nm	62	–	[82]
	Ag-TiO_{2-x}	flow reactor, xenon lamp, > 400 nm	45	–	[83]
	ZnAlFe-CO_3	laminar flow reactor, xenon lamp	56	93	[84]
	Mg_2Al-LDH	flow reactor, commercial UV lamp	42.1	87.2	[85]
	$ZnCo_2O_4$/rGO	flow reactor, halogen lamp	92.6	–	[86]
Carbon nitride based materials	Sb_2WO_6/g-C_3N_4	flow reactor, xenon lamp	68	–	[34]
	α-Fe_2O_3/g-C_3N_4	flow reactor, xenon lamp, > 400 nm	60.8	–	[35]
	g-C_3N_4	flow reactor, xenon lamp, > 420 nm	62	–	[28]
	g-C_3N_4/graphene oxide	flow reactor, metal halide lamp, > 420 nm	46.1	97.6	[29]
	Mo-g-C_3N_4/g-C_3N_4	flow reactor, metal halide lamp, > 420 nm	36	–	[30]
	g-C_3N_4/α-$Ni(OH)_2$	flow reactor, metal halide lamp, > 420 nm	51.3	100	[31]
	g-C_3N_4/Au/$ZnIn_2S_4$	flow reactor, xenon lamp	59.7	94.1	[36]
	$BaWO_4$/g-C_3N_4	flow reactor, LED	42.17	–	[87]
	BiOBr/g-C_3N_4	flow reactor, xenon lamp	63	96	[88]
	g-C_3N_4	flow reactor, tungsten halogen lamp, > 420 nm	41.84	–	[89]
	g-C_3N_4	flow reactor, LED, > 420 nm	40.3	–	[90]
	Pd-g-C_3N_4	flow reactor, tungsten halogen lamp, > 420 nm	51.5	97.8	[91]
	CH-CN	flow reactor, mercury lamp, > 400 nm	33	–	[92]
	g-$C_3N_4/BO_{0.2}N_{0.8}$	flow reactor, metal halide lamp, > 420 nm	30.2	97	[93]
	O-g-C_3N_4	flow reactor, tungsten halogen lamp, > 420 nm	45.5	–	[94]
	NCN/rGO/PI	flow reactor, xenon lamp, > 420 nm	60	–	[95]
	N-Vacancies g-C_3N_4	flow reactor, xenon lamp, > 420 nm	32.8	–	[96]
	N-Vacancies g-C_3N_4	flow reactor, xenon lamp, > 420 nm	81.97	–	[97]
	$AgVO_3$-g-C_3N_4	flow reactor, xenon lamp	55	–	[98]
	Au-g-C_3N_4	flow reactor, tungsten halogen lamp, > 420 nm	41	–	[99]
	g-C_3N_4-TiO_2	flow reactor, xenon lamp, > 420 nm	28	–	[100]
	O/La-g-C_3N_4	flow reactor, tungsten halogen lamp	50.4	–	[101]
	B-g-C_3N_4	flow reactor, halogen lamp, > 420 nm	44.1	–	[102]
	Bi-g-C_3N_4	flow reactor, tungsten halogen lamp, > 420 nm	60.8	–	[103]
	$SrCO_3$-g-C_3N_4	flow reactor, tungsten halogen lamp, > 420 nm	50.5	–	[104]
Other materials	CTF	flow reactor, LED	55	–	[105]
	CMP	flow reactor, LED	56	–	[106]

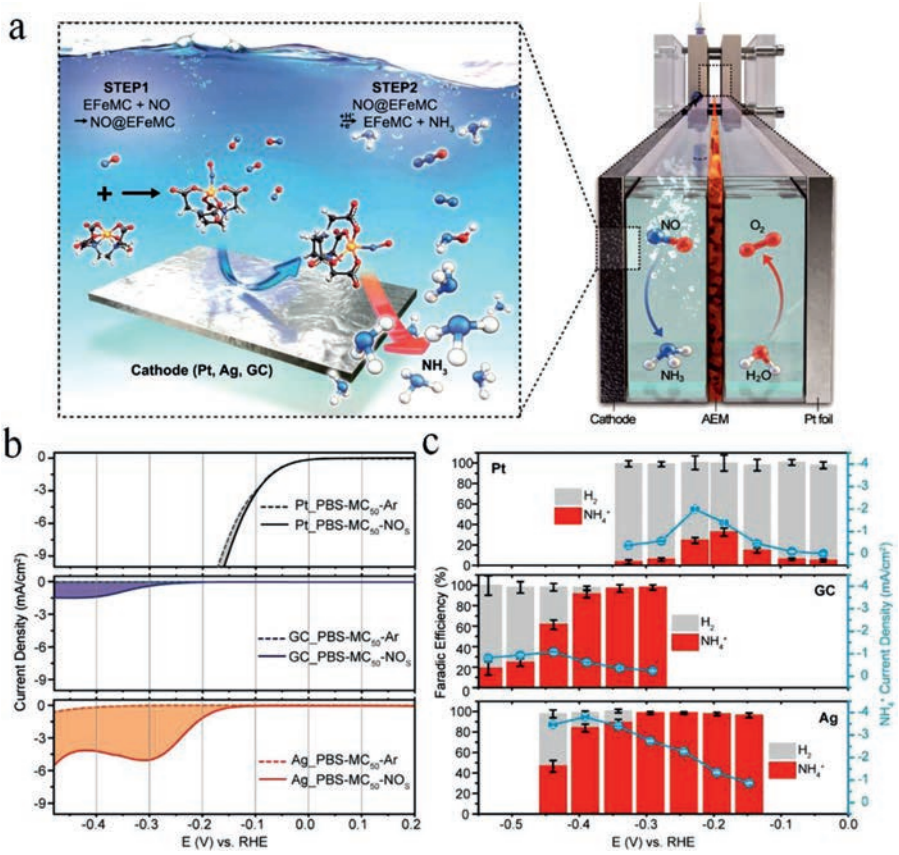

Fig. 6. Electrochemical NORR in PBS-MC_{50}-NO_s and PBS-MC_{50}-Ar electrolytes on different cathode materials: platinum (Pt), glassy carbon (GC), and silver (Ag). (a) Schematic diagram showing NO capture by FFeMC present in the electrolyte and its electrochemical reduction to ammonia. (b) Linear sweep voltammograms (LSVs) for Pt, GC, and Ag electrodes for the electrochemical NORR in PBS-MC_{50}-NO_s and PBS-MC_{50}-Ar electrolytes. (c) Faradic efficiencies and current densities for the formation of NH_4^+ in the potential range of −0.55 V to 0 V. Values were averaged, and error bars indicate the standard deviation ($n = 3$ replicates). Copied with permission [44]. Copyright 2020, American Chemical Society.

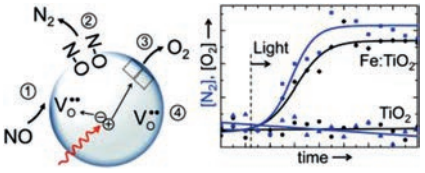

Fig. 7. Photocatalytic conversion of NO to N_2 and O_2 over Fe-doped TiO_2. The sample was irradiated with UV light, and the target pollutant was 100 ppm NO in He. Copied with permission [40]. Copyright 2012, American Chemical Society.

nanosheets with homogeneous C-doping (UC-BMO) by a hydrothermal process to enhance the photoinduced carries separation through internal electric field and negatively shift the CB of UC-BMO for the activation of molecular oxygen without any attenuation of light absorption simultaneously. Band-gap analysis based on DRS, VB-XPS and Mott–Schottky plot for different examples are shown in Figs. 8a-c. As revealed in Fig. 8d, the VB and CB of B-BMO is considered not enough for both water ($H_2O/^{\bullet}OH$, 2.38 V *vs.* NHE, pH=0) and oxygen ($O_2/^{\bullet}O_2^-$, −0.33 V *vs.* NHE, pH=0) activation, while, the obtained CB position (−0.46 V *vs.* NHE, pH = 0) of UC-BMO is negatively enough to transfer photogenerated electrons to oxygen and then activate molecular oxygen. For photocatalytic nitric oxide removal tests, UC-BMO exhibited 4.3 times higher than that of bulk BMO without obvious increasing of NO_2 production rate. Finally, the whole process of NO removal can be summarized as the following three steps (Fig. 9) based on the results of the radical scavenger studies.

Except for energy band engineering, construction of OVs which can facilitate the absorption and activation of O_2 for ROS generation and then enhance the oxidation of NO is an essential strategy. Wang *et al.* firstly investigated the impact of bromide ions (Br^-) on OVs construction on different facets of Bi_2MoO_6, and found that Br^- can boost and stabilize the OVs on (001) facets of Bi_2MoO_6, while hardly affect that on (010) facets [23]. As a result, BMO-001-Br exhibited dramatic enhancement in NO removal efficiency than that of BMO-001 (Fig. 10a), while no change was observed for BMO-010-Br. In addition, the effect of Br^- concentration and repeatability of BMO-001-Br were evaluated (Figs. 10b and c) as well as the detection of NO_3^- and NO_2 byproduct (Figs. 10d and e). More interestingly, near-infrared light ($\lambda = 730$ nm) induced photocatalytic NO removal was observed over BMO-001-Br (Fig. 10f), indicating the light absorption region was extended simultaneously. This work provides new insight into understanding the exogenous ions on construction and stabilization of OVs and the roles of OVs in photocatalytic NO removal.

Although surface oxygen vacancies can normally enhance photocatalytic activity, they suffer from instability and deactivation in continuous photocatalytic procedure. Taken Bi metal nanoparticle decorated $Bi_2O_2CO_3$ nanosheets with oxygen vacancy (Bi@OV-BOC) as model, Dong *et al.* found that O_2 and H_2O molecules would not fill into oxygen vacancies because they can be activated by Bi metal nanoparticle. In addition, the synergistic effect of Bi metal nanoparticles and oxygen vacancies could promote the completely oxidation of NO to NO_3^- instead of NO_2. As depicted in Fig. 11a, Bi@OV-BOC exhibited the highest NO removal efficiency because

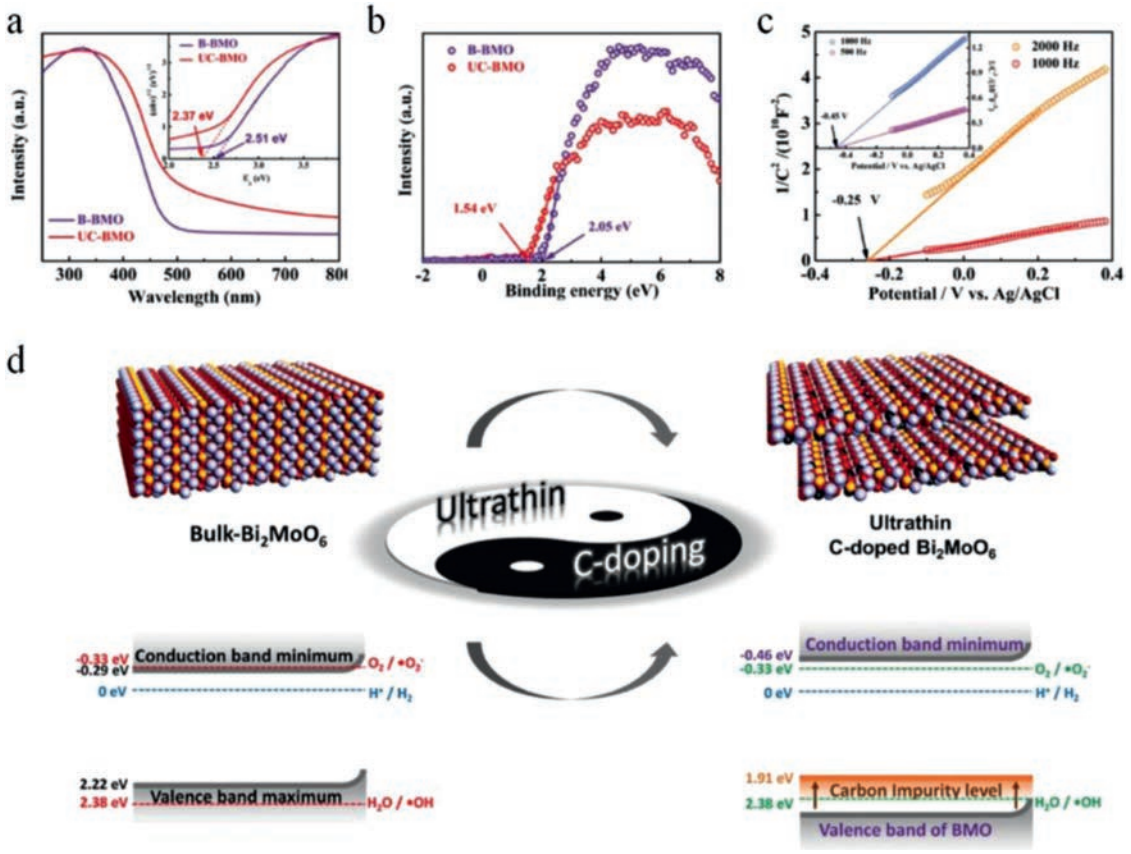

Fig. 8. (a) UV–vis absorption spectra, the corresponding Tauc plots (inset), and (b) valence-band XPS (VB-XPS) spectrum of the as-prepared samples. (c) The Mott–Schottky plots of B-BMO (inset) and UC-BMO in 0.5 mol/L Na_2SO_4 aqueous solution. (d) Schematic illustration of the bandgap engineering strategy and corresponding energy band diagram. Copied with permission [50]. Copyright 2017, John Wiley & Sons, Inc.

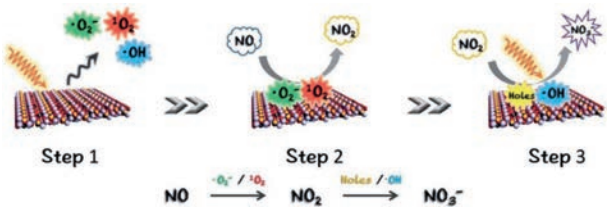

Fig. 9. The supposed steps of photocatalytic NO removal on UC-BMO. Copied with permission [50]. Copyright 2017, John Wiley & Sons, Inc.

of the co-effect of Bi metal nanoparticles and oxygen vacancies. To certify the influence of water on oxygen vacancies, water was used as dispersion solvent instead of ethanol, which resulted in the significant decrease in NO removal ratio for OV-BOC (Fig. 11b). This phenomenon is rationalized by the fact that H_2O filled into oxygen vacancies of OV-BOC (Fig. 11c). However, Bi@OV-BOC always keeps the same color and stable photocatalytic activity whatever the dispersion solvent is (Fig. 11c), indicating that Bi metal nanoparticles prevent H_2O molecules from filling into oxygen vacancies, and then the stability of Bi@OV-BOC was enhanced (Figs. 11d-f).

As mentioned above, the function of $^{\bullet}O_2^-$ in the photocatalytic oxidation process of NO ($NO + {}^{\bullet}O_2^- \rightarrow NO_3^-$ or $NO + {}^{\bullet}O_2^- \rightarrow NO_2$) is debatable. To clarify this issue, Li *et al.* investigated the influences of specific geometric structures of $^{\bullet}O_2^-$ on the reaction selectivity [18]. Taken BiOCl(001) with surface OV as model, they found that terminal end-on $^{\bullet}O_2^-$ favored the formation of NO_2 and the side-on $^{\bullet}O_2^-$ could oxide NO to NO_3^- based on DFT and experimental data. As can be seen in Fig. 12a, NO was oxidized to peroxynitrite (OONO-, a transient precursor toward the NO_2 formation) when NO approached the terminal end-on $^{\bullet}O_2^-$, and then release of gaseous NO_2 was favorable (pathway I). In contrast, direct oxidation of NO into NO_3^- could be operated without any barrier ($\Delta E = -3.10$ eV) over side-on bridging $^{\bullet}O_2^-$ (pathway II). In addition, charge density difference calculation was adopted to trace the interfacial charge transfer and uncover the remarkably promoted thermodynamics of NO oxidation by side-on bridging $^{\bullet}O_2^-$ (Figs. 12b-d).

Photocatalytic tests indicated that defect-free BiOCl was inefficient for NO removal under visible light irradiation (Fig. 13a). As for BiOCl-OV, up to 70% NO removal ratio was observed within 15 min and only 4 ppb NO_2 was detected which was expected, indicating the NO_3^- production selectivity exceeding 99%. In addition, Photocatalytic NO removal rates were linearly related with $^{\bullet}O_2^-$ in different concentrations (Fig. 13b). Based on reactive species trapping experiment, photocatalytic NO oxidation to nitrate was considered directly related to $^{\bullet}O_2^-$ generated via BiOCl intraband excitation and the generation of holes (O^-) and $^{\bullet}OH$ could be avoided (Fig. 13c). Besides, the influence of microstructure (nanospheres or nanosheets) on the long-term stability for NO removal was investigated (Fig. 13d).

Different form the above single electron-trapped center (V_O') in BiOCl (001), an archetypal F center (V"$_O$") that can localize two electrons over BiOCl (010) was designed to selectively oxide NO to nitrate with an interfacial charging-decharging process, as shown in the following Eqs. 36–40 [17]:

$$V''_O + O_2 \rightarrow V''_O\text{-}O_2^{2-} \quad (36)$$

$$V''_O - O_2^{2-} + NO \rightarrow V_O\text{-}NO_3^- + e^- \quad (37)$$

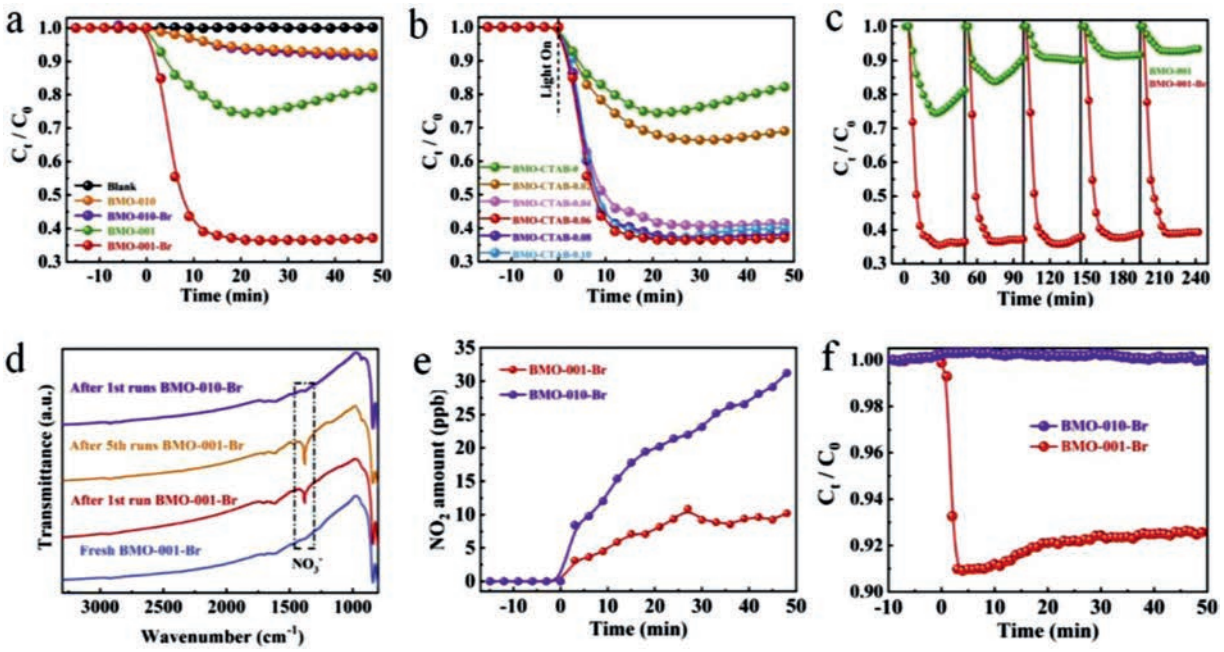

Fig. 10. Photocatalytic activities of as-prepared catalysts toward removal of NO under visible light irradiation (a), Photocatalytic activities of as-prepared Bi_2MoO_6 with different concentration of CTAB toward removal of NO under visible light irradiation (b). Cyclic NO removal tests with BMO-001 and BMO-001-Br under visible light irradiation (c). FTIR spectra of as-prepared Bi_2MoO_6 before and after irradiation (d). NO_2 generated by BMO-001-Br and BMO-010-Br during the photocatalysis (e) and the Photocatalytic activities of BMO-001-Br and BMO-010-Br toward removal of NO under near-infrared single wavelength LED light ($\lambda = 730$ nm) (f). Copied with permission [23]. Copyright 2020, Elsevier.

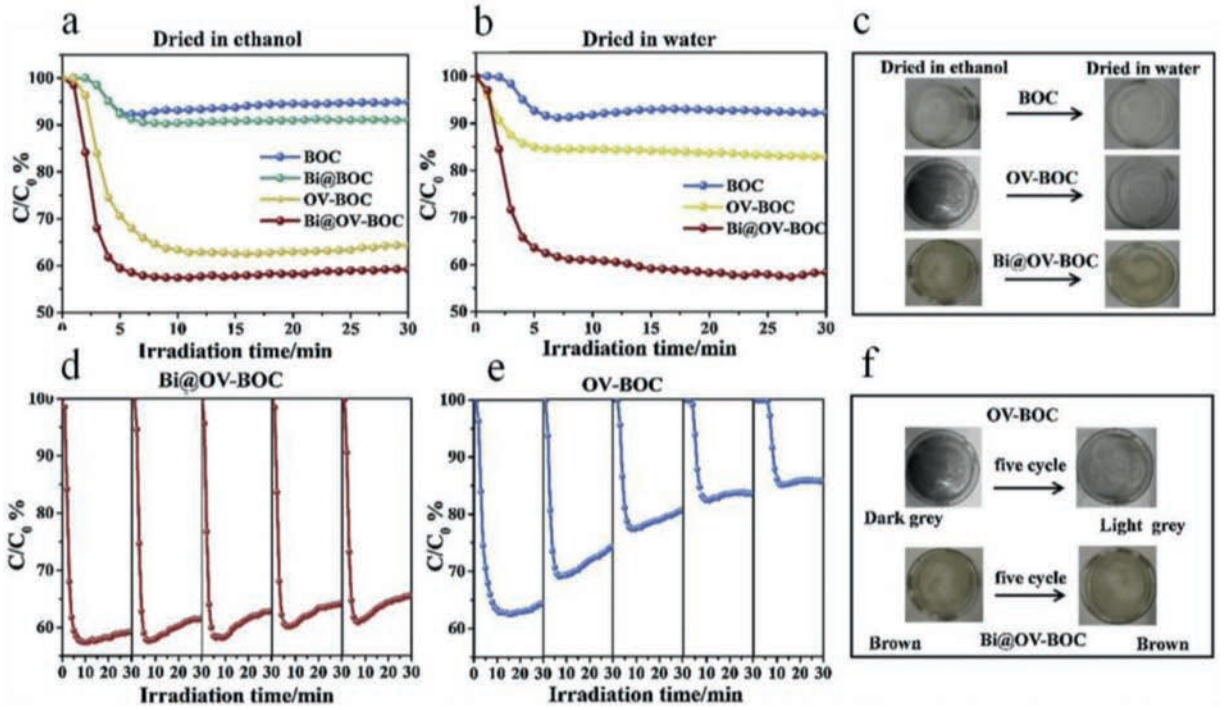

Fig. 11. Photocatalytic NO removal activity of the samples dried in ethanol (a); Photocatalytic activity for NO removal of the samples dried in water (b); The color of the sample dried in ethanol and water, respectively (c); Photocatalytic cycling tests for Bi@OV-BOC (d) and OV-BOC(e); Color change of the samples dried in ethanol before and after reaction (f). Copied with permission [57]. Copyright 2020, Elsevier.

$$V_O + e^- \rightarrow V_O' \quad (38)$$

$$V_O' + O_2 \rightarrow V_O' - {}^{\bullet}O_2^- \quad (39)$$

$$V_O' - {}^{\bullet}O_2^- + NO \rightarrow V_O - NO_3^- \quad (40)$$

It was found that direct oxidation of NO to NO_3^- was an exothermic process with a small energy barrier without forming any intermediates (Fig. 14a). In addition, V''_O was transformed into V_O' through electron back-donation along with O_2^{2-}-catalyzed NO oxidation (Figs. 14b-f). Fig. 15a showed the continuous flow reactor for photocatalytic NO oxidation tests. Control experiment

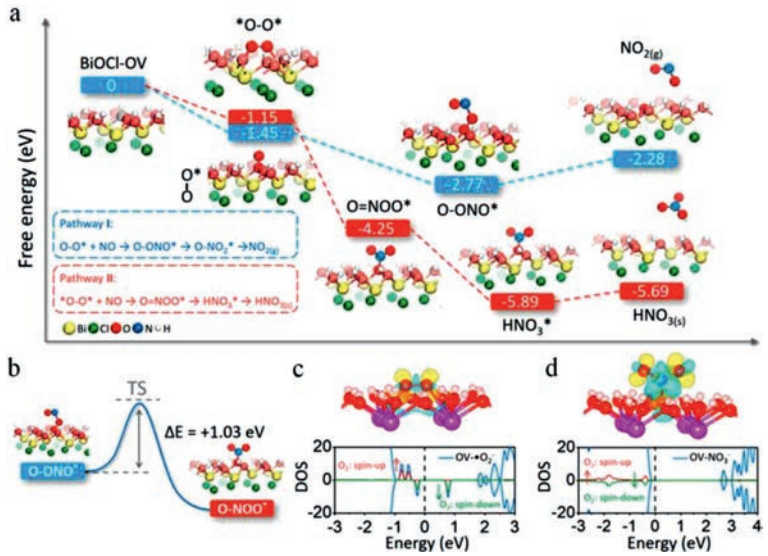

Fig. 12. (a) Free energy change against the reaction coordinate for the oxidation of NO by $^{\bullet}O_2^-$ on BiOCl (001) surface in different geometries. (b) Geometric transition from peroxynitrite to nitrate. TS represents transition state. Charge density difference and O_2 partial DOS of the BiOCl (001) surface adsorbed with (c) O_2 and (d) nitrate. The yellow and blue isosurfaces with an isovalue of 0.005 au represent charge accumulation and depletion in the space. The vertical dashed line in the DOS shows the VBM. Copied with permission [18]. Copyright 2018, American Chemical Society.

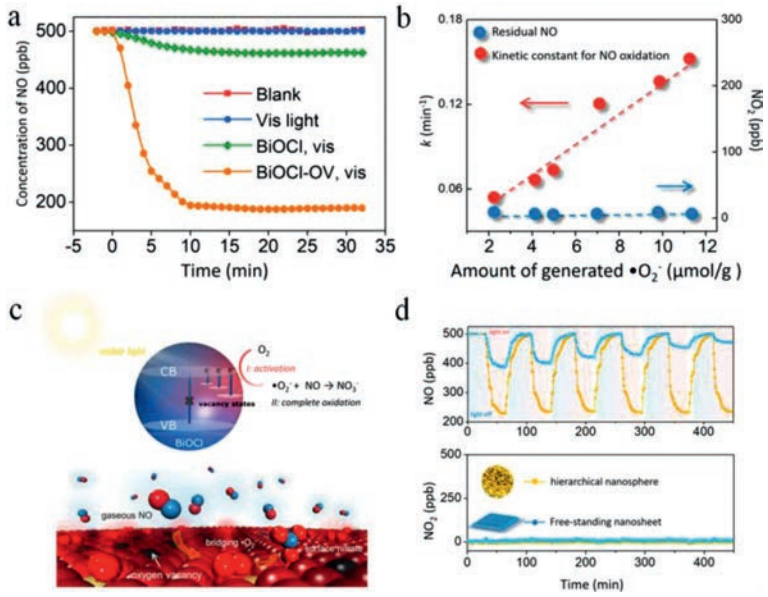

Fig. 13. (a) Photocatalytic NO removal over the as-prepared BiOCl under visible light. (b) Influence of generated $^{\bullet}O_2^-$ on the NO oxidation kinetic constants and the NO_2 concentration. (c) Schematic illustration of photocatalytic NO removal on BiOCl-OV. (d) Transient photocatalytic NO removal on BiOCl-OV. Copied with permission [18]. Copyright 2018, American Chemical Society.

exhibited that almost no activity was observed for all of the catalysts tested. However, 60% NO removal efficiency was detected for BOC-010-V"$_O$" (Fig. 15b), which was 1.8 times than that of BOC-001-V_O'. Meanwhile, the generation of NO_2 was suppressed to ~10% (Fig.15c). Finally, interfacial charging-discharging strategy accounts for oxidation of NO into nitrate with both high efficiency and selectivity was shown in Figs. 15d and e.

Except for the above-mentioned bandgap engineering and OV construction, fabrication of heterojunction based on different semiconductors with quick internal charge transfer is an efficient strategy to enhance the photoactivity of catalysts. Hu *et al*. synthesized a Z-scheme heterojunction (Fig. 16) of 2D/2D BP/MBWO nanosheets based on black phosphorus (BP) and monolayer Bi_2WO_6, and the optimal 12% BP/MBWO catalyst exhibited a NO removal ratio as high as 67%, which was much higher than that of MBWO (only 26%) [73]. The unexpected improvement for the photoactivity was attributed to efficient charge transfer and broad light harvesting range.

Recently, some metal-free organic semiconductors like g-C_3N_4, CMPs (conjugated microporous polymers), MOFs and COFs are hot materials in this field due to their unique visible light absorption property or pore structure. For example, three CMPs (Fig. 17) consisting of alternating electron-rich and electron-deficient units with ethynyl linker and changeable optical bandgaps were synthesized by Xiang *et al*., for which the structure-activity relationship was deeply investigated, and the highest NO removal efficiency reached to 56% [106]. Zhang *et al*. found that the H atoms of α-$Ni(OH)_2$ improve the adsorption and activation of O_2 and oxygen

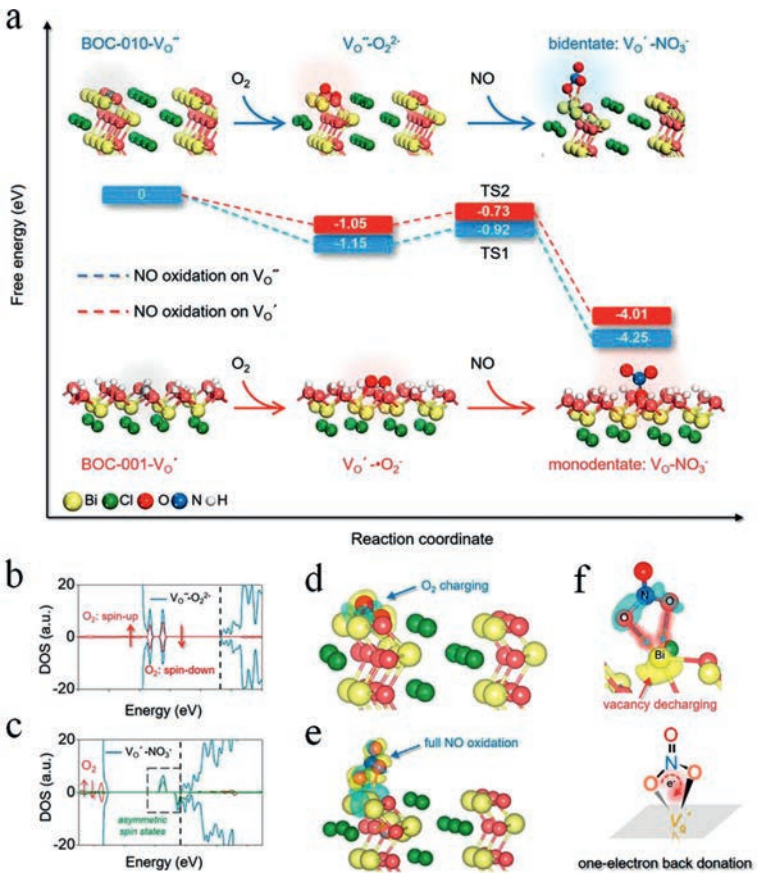

Fig. 14. (a) Free energy change during O_2^{2-}- and $^{\cdot}O_2^-$-mediated NO oxidation on the VO of BOC-010 and BOC-001, respectively. TS represents the transition state. DOS of (b) O_2^{2-}-adsorbed (c) NO_3^--adsorbed BOC-010 with VO. Vertical dashed line in the DOS shows the CB minimum. Charge density difference of (d) O_2^{2-}-adsorbed (e) NO_3^--adsorbed BOC-010 with VO. (f) Regional charge density difference between O_2^{2-} and VO on BOC-010. The yellow and blue isosurfaces with an isovalue of 0.005 au represent spatial charge accumulation and depletion, respectively. Copied with permission [17]. Copyright 2019, American Chemical Society.

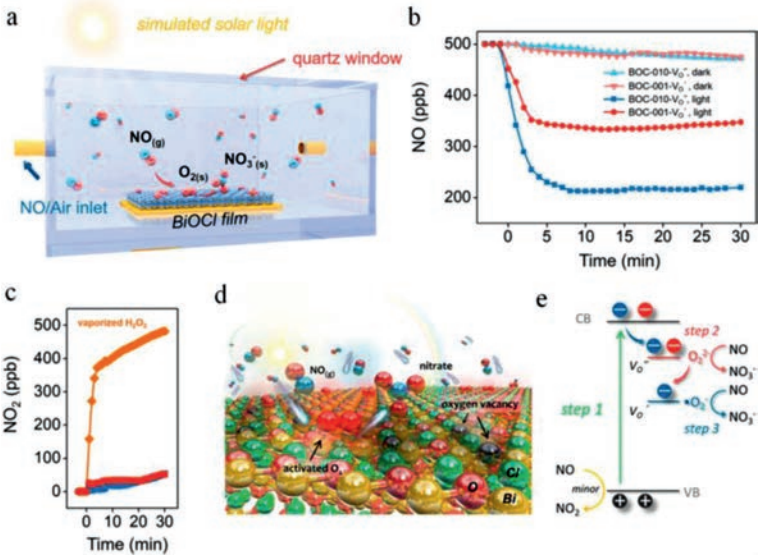

Fig. 15. (a) Reaction chamber for the continuous indoor NO removal. (b) Photocatalytic NO removal over BiOCl under simulated solar light and (c) the accompanying NO_2 generation. (d) Schematic illustration of NO removal on BOC-010-VO'' and (e) the corresponding electronic excitation process. Copied with permission [17]. Copyright 2019, American Chemical Society.

atoms to promote NO and NO_2 oxidized to nitrate, and the fabricated g-C_3N_4/α-Ni$(OH)_2$ showed enhanced NO removal ratio of 51.3% without any toxic NO_2 generation (Fig. 18) [31].

Generally speaking, gaseous NO is inactivated due to the preferential adsorption of O_2 rather than NO in most reported literatures. And the total NO removal efficiency could be further improved if NO can be activated simultaneously. To realize this aim, an Au/CeO_2 photocatalyst with abundant OVs was designed by Shang *et al*, in which O_2 and NO were adsorbed and activated into $^{\cdot}O_2^-$ and NO^+ on OV and Au nanoparticle respectively [38]. As indicated in Fig. 19, a *OONO structure was formed with overcoming the 0.11 eV barrier when O_2 and NO were activated on the inter-

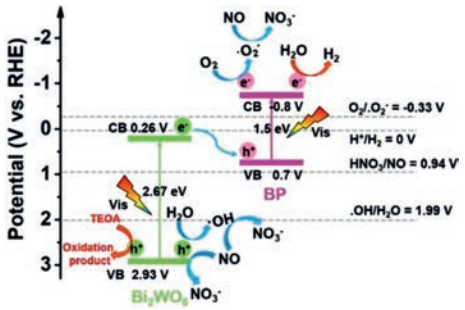

Fig. 16. Photocatalytic mechanism of NO removal and water splitting by BP/MBWO heterojunction under visible-light irradiation (the various redox potentials *versus* RHE). Copied with permission [73]. Copyright 2019, John Wiley & Sons, Inc.

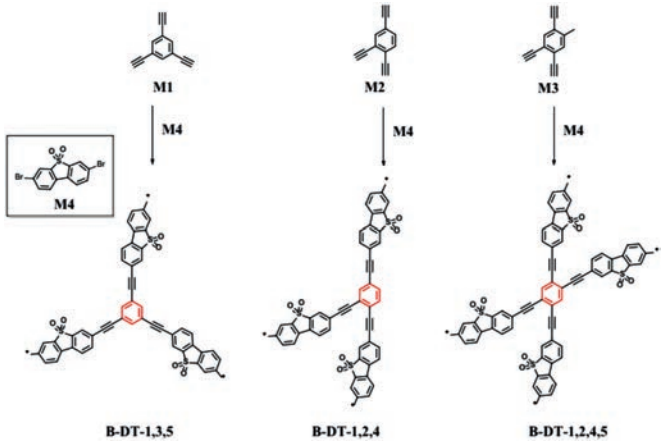

Fig. 17. Structures of monomers and synthesis of CMP photocatalysts by Sonogashira cross-coupling polycondensation. Copied with permission [106]. Copyright 2018, Elsevier.

faces of Au/CeO_2. And then *OONO precursor transformed to nitrate with releasing 1.10 eV energy spontaneously. The DFT results suggested that photocatalytic NO removal on Au/CeO_2 surfaces occurs *via* Langmuir-Hinshelwood (L-H) mechanism, which was different from that of CeO_2 catalyst undergoing an Eley-Rideal (E-R) mechanism, where inactivated NO was attacked by active $^{\bullet}O_2^-$. In addition, Dong *et al.* reported that nitrogen defects were introduced into the framework of g-C_3N_4 by heating g-C_3N_4 powder in the hydrogen atmosphere, and nitrogen atoms were partially removed with hydrogen. The N defects sites can promote the formation of NO^+ reaction intermediate, and then accelerated the photocatalytic NO oxidation reaction [89], as shown in Fig. 20.

In a word, NO removal by environmentally friendly photocatalytic technology is promising in consideration of direct utilization of clean solar energy and numerous efforts have been made in the past decades [107–111]. Especially, low concentration of NO (~500–600 ppb) can be treated by this method under mild conditions with high efficiency. However, direct converting NO into valuable NH_3 is still blank, and production of undesirable NO_2 is usually inevitable. In addition, single-atom catalysts, which have realized their value in series of energy and environment issues, are ignored in the development trail of this field.

4. Conclusions and perspectives

In summary, selective catalytic oxidation or reduction of nitrogen oxides is vital to the global environment and human health. In this review, the recent main achievements in the field of nitrogen oxides removal are discussed and summarized, including thermo-catalysis, electro-catalysis and photo-catalysis. In spite of significant progress have been achieved, there are still issues requiring complete solving: (1) The standard evaluation and reaction system should be established, especially reactors, energy source and detection equipment. (2) Exploring more efficient catalyst for NO removal with high selectivity. (3) Establishing novel and highly efficient methods to convert NO into value-added products such as NH_3 other than harmless N_2 or NO_3^-. (4) The mechanism investigation of NO removal pathway and structure-activity relationship. (5) Designing practical instruments to purify NO in urban atmosphere. For NH_3-SCR, novel strategy or catalyst should be explored to carry out NH_3-SCR under lower temperature or even ambient condition. For many cases, the lower outlet temperature of industrial boilers as well as impurities including SO_2 and H_2O will decrease the catalytic activities of NH_3-SCR catalysts. In addition, these catalysts are easy to be poisoned by SO_2 present in boiler

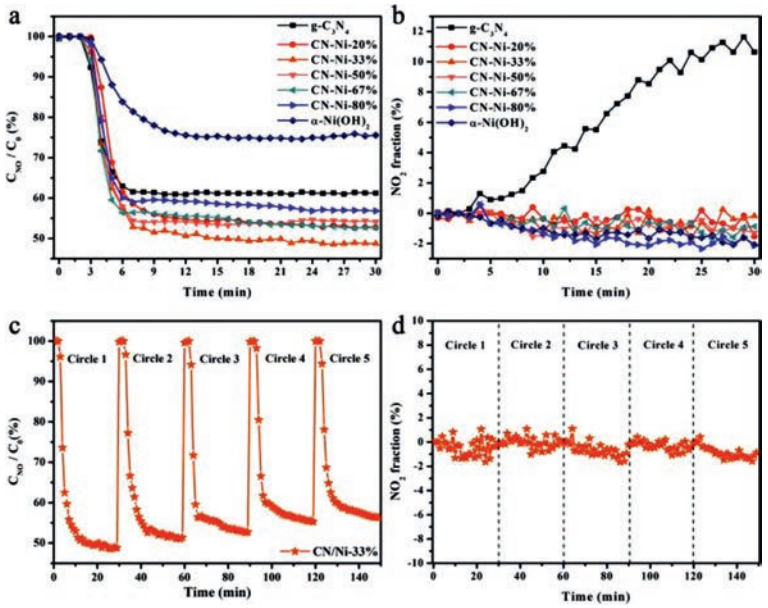

Fig. 18. NO remove ratio (a) and NO_2 fraction (b) over different samples; NO remove ratio (c) and NO_2 fraction (d) of recycle experiment. Copied with permission [31]. Copyright 2020, Elsevier.

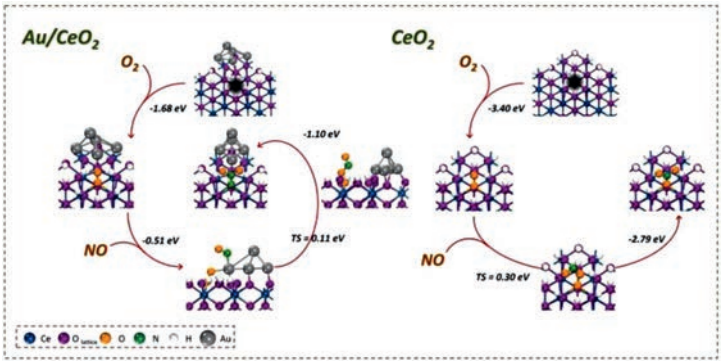

Fig. 19. DFT calculations for NO oxidation on the Au/CeO_2 and CeO_2 with (100) surface exposed. Copied with permission [38]. Copyright 2020, Elsevier.

flue gas. Therefore, the SO_2-tolerance should be taken into consideration preferentially. By the way, the investigation on adsorption and activation of NO on NH_3-SCR catalyst is urgent.

Although numerous reports are focused on semiconductor based photocatalytic NO removal, the selectivity of nitrogen oxides removal for most photocatalyst are prominent problem and the formation of NO_2 is unavoidable. Additionally, the reported catalytic mechanisms for photocatalytic NO removal are various, which need further investigation. For example, OV is generally considered to play significant role in O_2 adsorption and activation, however, the controllable and quantitative fabrication of OV on semiconductors as well as systematic investigation of OV on NO removal efficiency ruling out other factors has not been clearly investigated. Moreover, the biggest issue in this field is insufficient practical application study, that is, the evaluation of the purification of the present photocatalyst on urban atmosphere is urgent. For emerging electro-catalytic NH_3 production from NO reduction, the collection of efficient catalyst and clarifying relative mechanism is of great significance.

In addition, this field is also filled with opportunities. Herein, some constructive opinions on NO removal are proposed. Firstly, coupling of solar energy, thermal energy and electrical energy is scarce in nitrogen oxides removal, in which environmentally friendly photothermo- and photoelectro-catalysis are promising, which have been proven to be extremely efficient strategy in other fields. Very recently, some groundbreaking works on gas-phase photoelectron-catalytic oxidation of NO (~ 550 ppb) are reported using TiO_2-based photocatalyst with high efficiency [112,113], and the typical experimental setup are displayed in Fig. 21. This novel technology can overcome the disadvantage of photocatalysis, which suffers from rapid recombination of photogenerated electron holes. Secondly, nitrogen oxides are usually converted into uneconomic N_2 or NO_3^- in most reports. Direct electrochemical ammonia synthesis from nitric oxide has been realized very recently, which should be given priority in the future considering the value of NH_3. Thirdly, exploring single atom catalyst suitable for NO removal is urgent, which is one of the hottest materials in the current state. Fourthly, coupling removal of NO and NH_3 through photocatalytic technology may enhance the purification of pollutants in atmosphere under mild conditions. Finally, the investigation of solving practical environmental and ecological problems, such as urban atmosphere, using the aforementioned technologies especially solar energy driven photo-catalysis and photoelectro-catalysis should be the prior choice.

Declaration of competing interest

The authors declare that they have no known competing financial interests or personal relationships that could have appeared to influence the work reported in this paper.

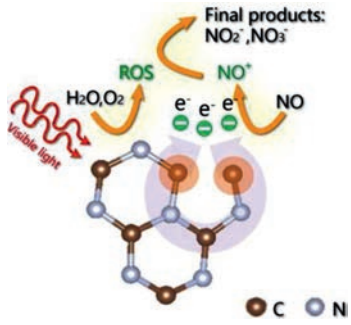

Fig. 20. Illustration of photocatalytic NO removal on N defects sites containing g-C_3N_4. Copied with permission [89]. Copyright 2020, Elsevier.

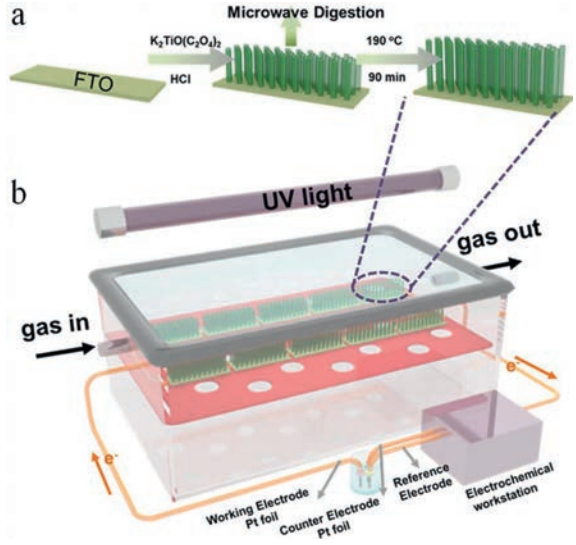

Fig. 21. Schematic illustrations of the fabrication route for TiO_2-NRs/FTO photoanodes (a) and the gas-phase PEC oxidation reactor (b). Copied with permission [112]. Copyright 2020, American Chemical Society.

Acknowledgments

This work was financially supported by National Natural Science Foundation of China (Nos. 21703075, 51872107, 52073110, 51902121), Natural Science Foundation of Hubei Province (No. 2020CFB694) and Fundamental Research Funds for the Central Universities (No. 2662020LXPY005).

References

[1] J. Becher, D.F. Sanchez, D.E. Doronkin, et al., Nat. Catal. 4 (2020) 46–53.
[2] P. Zhang, Y. Huang, Y. Rao, et al., Chem. Eng. J. 406 (2021) 126910.
[3] F. Rao, G. Zhu, W. Zhang, et al., Appl. Catal. B: Environ. 281 (2021) 119481.
[4] C. Yuan, R. Chen, J. Wang, et al., J. Hazard. Mater. 400 (2020) 123174.
[5] J. Hu, C. Zhai, M. Zhu, Chin. Chem. Lett. 32 (2021) 1348–1358.
[6] H. Wu, C. Yuan, R. Chen, et al., ACS Appl. Mater. Interfaces 12 (2020) 43741–43749.
[7] J.K. Lai, I.E. Wachs, ACS Catal. 8 (2018) 6537–6551.
[8] G. Xu, J. Ma, L. Wang, et al., ACS Catal. 9 (2019) 10489–10498.
[9] H. Kubota, C. Liu, T. Toyao, et al., ACS Catal. 10 (2020) 2334–2344.
[10] A. Oda, H. Shionoya, Y. Hotta, et al., ACS Catal. 10 (2020) 12333–12339.
[11] B. Wang, M. Wang, L. Han, et al., ACS Catal. 10 (2020) 9034–9045.
[12] Z. Liu, G. Sun, C. Chen, et al., ACS Catal. 10 (2020) 6803–6809.
[13] Y. Zhou, J. He, J. Lu, Y. Liu, Y. Zhou, Chin. Chem. Lett. 31 (2020) 2623–2626.
[14] R. Zhang, W. Jian, Z. Yang, F. Bai, Chin. Chem. Lett. 31 (2020) 2319–2324.
[15] H. Qiang, T. Chen, Z. Wang, et al., Chin. Chem. Lett. 31 (2020) 3225–3229.
[16] S. Hu, Y. Yu, Y. Guan, et al., Chin. Chem. Lett. 31 (2020) 2839–2842.
[17] H. Li, H. Shang, Y. Li, et al., Environ. Sci. Technol. 53 (2019) 6964–6971.
[18] H. Li, H. Shang, X. Cao, et al., Environ. Sci. Technol 52 (2018) 8659–8665.
[19] G. Cheng, X. Liu, X. Song, et al., Appl. Catal. B: Environ. 277 (2020) 119196.
[20] M. Çağlayan, M. Irfan, K. Ercan, Y. Kocak, E. Ozensoy, Appl. Catal. B: Environ. 263 (2020) 118227.
[21] H. Shang, M. Li, H. Li, et al., Environ. Sci. Technol. 53 (2019) 6444–6453.
[22] H. Wu, R. Chen, H. Wang, et al., Catal. Sci. Technol. 10 (2020) 826–834.
[23] S. Wang, X. Ding, N. Yang, et al., Appl. Catal. B: Environ. 265 (2020) 118585.
[24] H. Wang, W. Cui, X. Dong, et al., Chem. Eng. J. 390 (2020) 124609.
[25] Y. Liu, Y. Zhou, S. Yu, ACS Appl. Nano Mater. 3 (2020) 772–781.
[26] Z. Zhou, Y. Li, M. Li, Y. Li, S. Zhan, Chin. Chem. Lett. 31 (2020) 2698–2704.
[27] Q. Chen, X. Cheng, H. Long, Y. Rao, Chin. Chem. Lett. 31 (2020) 2583–2590.
[28] M. Zhou, G. Dong, J. Ma, et al., Appl. Catal. B: Environ. 273 (2020) 119007.
[29] R. Zhang, A. Zhang, Y. Yang, et al., J Hazard. Mater. 397 (2020) 122822.
[30] R. Zhang, A. Zhang, Y. Cao, et al., Chem. Eng. J. 401 (2020) 126028.
[31] R. Zhang, T. Ran, Y. Cao, et al., Chem. Eng. J. 382 (2020) 123029.
[32] Y. Xing, X. Wang, S. Hao, et al., Chin. Chem. Lett. 32 (2021) 13–20.
[33] M. Ding, J. Zhou, H. Yang, et al., Chin. Chem. Lett. 31 (2020) 71–76.
[34] Y. Ren, Y. Li, X. Wu, J. Wang, G. Zhang, Chin. J. Catal. 42 (2021) 69–77.
[35] Y. Geng, D. Chen, N. Li, et al., Appl. Catal. B: Environ. 280 (2021) 119409.
[36] G. Zhang, X. Zhu, D. Chen, et al., Environ. Sci. Nano 7 (2020) 676–687.
[37] Q. Chen, H. Long, M. Chen, et al., Appl. Catal. B: Environ. 272 (2020) 119008.
[38] H. Shang, S. Huang, H. Li, et al., Chem. Eng. J. 386 (2020) 124047.
[39] S. Roy, M. Hegde, N. Ravishankar, G. Madras, J. Phys. Chem. C 111 (2007) 8153–8160.
[40] Q. Wu, R. Krol, J. Am. Chem. Soc. 134 (2012) 9369–9375.
[41] H.J. Chun, V. Apaja, A. Clayborne, K. Honkala, J. Greeley, ACS Catal 7 (2017) 3869–3882.
[42] Z. Wang, J. Zhao, J. Wang, C. Cabrera, Z. Chen, J. Mater. Chem. A 6 (2018) 7547–7556.
[43] J. Long, S. Chen, Y. Zhang, et al., Angew. Chem. Int. Ed. 59 (2020) 9711–9718.
[44] D. Kim, D. Shin, J. Heo, et al., ACS Energy Lett. 5 (2020) 3647–3656.
[45] S. Wang, F. Ichihara, H. Pang, H. Chen, J. Ye, Adv. Funct. Mater. 28 (2018) 1803309.
[46] Y.S. Mok, Chem. Eng. J. 118 (2006) 63–67.
[47] Y. Liu, J. Zhang, C. Zhang, Y. Zhang, L. Zhao, Chem. Eng. J. 162 (2010) 1006–1011.
[48] R. Hao, Y. Zhao, Energy Fuels 30 (2016) 2365–2372.
[49] X. Ding, W. Ho, J. Shang, L. Zhang, Appl. Catal. B: Environ. 182 (2016) 316–325.
[50] S. Wang, X. Ding, X. Zhang, et al., Adv. Funct. Mater. 27 (2017) 1703923.
[51] M.M. Mason, Z. Lee, M. Vasiliu, I. Wachs, D. Dixon, ACS Catal. 10 (2020) 13918–13931.
[52] S. Deng, T. Meng, B. Xu, et al., ACS Catal. 6 (2016) 5807–5815.
[53] J. Liao, K. Li, H. Ma, et al., Chin. Chem. Lett. 31 (2020) 2737–2741.
[54] M. Kou, Y. Deng, R. Zhang, et al., Chin. J. Catal. 41 (2020) 1480–1487.
[55] W. Huo, T. Cao, W. Xu, et al., Chin. J. Catal. 41 (2020) 268–275.
[56] R. Chen, H. Wang, H. Wu, et al., Chin. J. Catal. 41 (2020) 710–718.
[57] P. Chen, H. Liu, Y. Sun, et al., Appl. Catal. B: Environ. 264 (2020) 118545.
[58] M. Chen, X. Li, Y. Huang, et al., Appl. Surf. Sci. 513 (2020) 145775.
[59] G. Zhu, M. Hojamberdiev, S. Zhang, S. Din, W. Yang, Appl. Surf. Sci. 467-468 (2019) 968–978.
[60] Z. Zhao, Y. Cao, F. Dong, et al., Nanoscale 11 (2019) 6360–6367.
[61] J. Zhang, G. Zhu, S. Li, et al., ACS Appl. Mater. Interfaces 11 (2019) 37822–37832.
[62] L. Wang, K. Xu, W. Cui, et al., Adv. Funct. Mater. 29 (2019) 1808084.
[63] Y. Sun, J. Liao, F. Dong, S. Wu, L. Sun, Chin. J. Catal. 40 (2019) 362–370.
[64] M. Sun, W. Zhang, Y. Sun, Y. Zhang, F. Dong, Chin. J. Catal. 40 (2019) 826–836.
[65] M. Sun, X. Dong, B. Lei, et al., Nanoscale 11 (2019) 20562–20570.
[66] X. Shi, P. Wang, W. Li, et al., Appl. Catal. B: Environ. 243 (2019) 322–329.
[67] M. Ran, H. Wang, W. Cui, et al., ACS Appl. Mater. Interfaces 11 (2019) 47984–47991.
[68] Y. Lu, Y. Huang, Y. Zhang, et al., Chem. Eng. J. 363 (2019) 374–382.
[69] X. Li, W. Zhang, J. Li, et al., Appl. Catal. B: Environ. 241 (2019) 187–195.
[70] J. Li, R. Chen, W. Cen, et al., Chem. Eng. J. 375 (2019) 122026.
[71] W.C. Huo, X. Dong, J. Li, et al., Chem. Eng. J. 361 (2019) 129–138.
[72] W. Huo, W. Xu, T. Cao, et al., Appl. Catal. B: Environ. 254 (2019) 206–213.
[73] J. Hu, D. Chen, et al., Angew Chem. Int. Ed. 58 (2019) 2073–2077.
[74] P. Chen, Y. Sun, H. Liu, et al., Nanoscale 11 (2019) 2366–2373.
[75] H. Wang, Y. Sun, G. Jiang, et al., Environ. Sci. Technol. 52 (2018) 1479–1487.
[76] H. Wang, Y. Sun, W. He, et al., Nanoscale 10 (2018) 15513–15520.
[77] Y. Lu, Y. Huang, Y. Zhang, et al., Appl. Catal. B: Environ. 231 (2018) 357–367.
[78] P. Zhu, X. Yin, X. Gao, et al., Chin. J. Catal. 42 (2021) 175–183.
[79] C. Yuan, W. Cui, Y. Sun, et al., Chin. Chem. Lett. 31 (2020) 751–754.
[80] J. Wang, Y. Asakura, S. Yin, J. Hazard. Mater. 396 (2020) 122709.
[81] X. Tan, G. Qin, G. Cheng, et al., Catal. Sci. Technol. 10 (2020) 6923–6934.
[82] Y. Duan, J. Luo, S. Zhou, et al., Appl. Catal. B: Environ. 234 (2018) 206–212.
[83] Y. Duan, M. Zhang, L. Wang, et al., Appl. Catal. B: Environ. 204 (2017) 67–77.
[84] A. Pastor, F. Rodriguez-Rivas, G. Miguel, et al., Chem. Eng. J. 387 (2020) 124110.
[85] X. Lv, J. Zhang, X. Dong, et al., Appl. Catal. B: Environ. 277 (2020) 119200.
[86] S. Xiao, D. Pan, R. Liang, et al., Appl. Catal. B: Environ. 236 (2018) 304–313.
[87] C. Wang, M. Fu, J. Cao, et al., Chem. Eng. J. 385 (2020) 123833.
[88] D. Liu, D. Chen, N. Li, et al., Angew Chem. Int. Ed. 59 (2020) 4519–4524.
[89] J. Liao, W. Cui, J. Li, et al., Chem. Eng. J. 379 (2020) 122282.
[90] Y. Li, M. Gu, M. Zhang, et al., Chem. Eng. J. 389 (2020) 124421.
[91] K. Li, Y. He, P. Chen, et al., J. Hazard. Mater. 392 (2020) 122357.
[92] Z. Gu, Z. Cui, Z. Wang, et al., Appl. Catal. B: Environ. 279 (2020) 119376.
[93] Y. Cao, R. Zhang, Q. Zheng, et al., ACS Appl. Mater. Interfaces. 12 (2020) 34432–34440.
[94] J. Yi, J. Liao, K. Xia, et al., Chem. Eng. J. 370 (2019) 944–951.
[95] L. Yang, P. Wang, J. Yin, et al., Appl. Catal. B: Environ. 250 (2019) 42–51.
[96] Z. Wang, Y. Huang, M. Chen, et al., ACS Appl. Mater. Inter. 11 (2019) 10651–10662.
[97] S. Wan, M. Ou, Y. Wang, et al., Appl. Catal. B: Environ. 258 (2019) 118011.
[98] D. Liu, D. Chen, N. Li, et al., Appl. Catal. B: Environ. 243 (2019) 576–584.
[99] K. Li, W. Cui, J. Li, et al., Chem. Eng. J. 378 (2019) 122184.
[100] Y. Huang, P. Wang, Z. Wang, et al., Appl. Catal. B: Environ. 240 (2019) 122–131.
[101] P. Chen, H. Wang, H. Liu, et al., Appl. Catal. B: Environ. 242 (2019) 19–30.
[102] J. Cao, J. Zhang, X. Dong, et al., Appl. Catal. B: Environ. 249 (2019) 266–274.
[103] G. Jiang, X. Li, M. Lan, et al., Appl. Catal. B: Environ. 205 (2017) 532–540.
[104] W. Cui, J. Li, F. Dong, et al., Environ. Sci. Technol. 51 (2017) 10682–10690.
[105] M. Liu, K. Jiang, X. Ding, et al., Adv. Mater. 31 (2019) 1807865.
[106] Y. Xiang, X. Zhang, X. Wang, et al., J. Catal. 357 (2018) 188–194.
[107] L. Mao, X. Cai, M. Zhu, Rare Met. 40 (2021) 1067–1076.
[108] Y. Cao, Q. Zheng, Z. Rao, et al., Chin. Chem. Lett. 31 (2020) 2689–2692.
[109] J. Liao, K. Li, H. Ma, et al., Chin. Chem. Lett. 31 (2020) 2737–2741.
[110] H. Ma, Y. He, X. Li, et al., Appl. Catal. B: Environ. 292 (2021) 120159.
[111] R. Sun, C. He, L. Fu, et al., Chin. Chem. Lett. 33 (2022) 527–532.
[112] W. Dai, Y. Tao, H. Zou, et al., Environ. Sci. Technol. 54 (2020) 5902–5912.
[113] S. Xiao, Z. Wan, J. Zhou, et al., Environ. Sci. Technol. 53 (2019) 7145–7154.